A Cost-Effective Dual-Independent-Output IPT System With Flexible Adjustment Capability for Industrial Power Supplies

Jiabin Wang, Lin Yang, Ronghuan Xie, *Graduate Student Member, IEEE*, Chao Liu, Wei Xu, Yizhan Zhuang, *Member, IEEE*, and Yiming Zhang, *Senior Member, IEEE*

***Abstract*—Research on wireless power transfer (WPT) systems, especially single-input multiple-output (SIMO) designs, has attracted significant interest due to their practicality. Nevertheless, existing multiple-output WPT systems face various challenges, including the inability to independently control the output levels at each port, reliance on specific decoupling coil structures, and poor space utilization. To address these issues, this article introduces a novel compensation topology capable of achieving independently adjustable dual constant voltage (CV) outputs exploiting its inherent structural attributes. The proposed system employs fewer passive compensation components, thereby reducing its volume and cost. Furthermore, this design does not require complex closed-loop control strategies, simplifying the difficulty of controller design. Instead, it simply requires adjustments to the compensation component parameters to achieve the desired dual CV output levels, thereby ensuring system flexibility. Initially, a theoretical analysis is conducted, followed by simulation verification, and finally, an experimental prototype is constructed to validate the feasibility of the proposed system.**

***Index Terms*—Dual constant voltage (CV) outputs, single-input multiple-output (SIMO), wireless power transfer (WPT).**

I. Introduction

INDUCTIVE power transfer (IPT) technology has become an essential branch of the development of wireless power transfer (WPT), providing various application scenarios, such as underwater charging [1], [2], [3], implantable medical devices [4], [5], [6], consumer electronics [7], [8], [9], and industrial power supplies [10], [11], [12]. The widespread adoption across diverse industries highlights the technology's versatility and its ability to solve speciffc power transfer challenges. With the development of the power industry, there is an increasing demand for designs that can provide different voltage outputs simultaneously, such as dc motor drives, flash drives, and automated guided vehicles. Therefore, multiple-output technology has emerged as a critical research area of IPT.

To meet system design requirements for multiple outputs, Hu et al. [13] and Matthew [14] adopted the most direct method of cascading dc–dc converters. Obviously, it takes up a lot of space and causes additional power losses. The multiple transmitters and multiple receivers structures are proposed in [15] and [16] to achieve independent multiple outputs without relying on dc–dc converters. Nevertheless, the above methods still face the problems of relatively large space occupation and high cost. In addition, cross-coupling among transmitters and receivers complicates the design process due to its impact on system output. In order to reduce spatial requirements, Ahn and Mercier [17] suggested a configuration with the single transmitter and dual receivers, whereas it also faces the same problem of cross-coupling interference between coils like [15] and [16]. To alleviate this problem, the decoupling coils design methods [18] and [19] are introduced to eliminate interference on the system output caused by cross-coupling between receiving coils. Unfortunately, when the system input voltage is determined, the magnitudes of the dual output voltages are determined by the ratio of corresponding mutual inductances between coils. This undoubtedly complicates the design of system parameters and brings challenges to flexibly adjusting the output voltage level. From another perspective of decoupling, Mai et al. [20] adopted a circuit-based decoupling method to avoid the influence of cross-coupling between receiving coils. However, achieving complete decoupling requires maintaining a fixed current ratio of the receivers, which means that the multiple outputs of the system are not allowed to be adjusted independently. To further improve the flexibility of the system, the authors in [21] and [22] propose single-input multiple-output (SIMO) IPT systems with the insertion of a single T resonant circuit that enables dual constant current (CC) outputs with independently adjustable levels utilizing the single transmitting and receiving coil structure. Furthering the method mentioned above, Li et al. [22] developed a dual T resonant

Received 18 February 2025; revised 13 June 2025; accepted 15 July 2025. Date of publication 17 July 2025; date of current version 27 August 2025. This work was supported in part by the National Natural Science Foundation of China under Grant 52107183 and in part by the Natural Science Foundation of Fujian Province under Grant 2022J06011. Recommended for publication by Associate Editor S. Tian. *(Corresponding authors: Yiming Zhang; Lin Yang.)*

Jiabin Wang, Ronghuan Xie, Chao Liu, Wei Xu, Yizhan Zhuang, and Yiming Zhang are with the Fujian Key Laboratory of New Energy Generation and Power Conversion, School of Electrical Engineering and Automation, Fuzhou University, Fuzhou 350108, China (e-mail: wangjiabin@stu.htu.edu.cn; 230127018@fzu.edu.cn; 220110002@fzu.edu.cn; 230120032@fzu.edu.cn; zyz_joe@fzu.edu.cn; zym@fzu.edu.cn).

Lin Yang is with the College of Electronic and Electrical Engineering, Academician Workstation of Electromagnetic Wave Engineering of Henan Province, Henan Normal University, Xinxiang 453007, China (e-mail: yang_lin@whu.edu.cn).

Color versions of one or more figures in this article are available at https://doi.org/10.1109/TPEL.2025.3590266.

Digital Object Identifier 10.1109/TPEL.2025.3590266

circuit by connecting the *CLC* circuit to the output port of the *LCL* circuit, facilitating the achievement of dual constant voltage (CV) outputs. Nonetheless, achieving dual CV outputs necessitates cascading two sets of dual *T* resonant circuits behind the *LCC*-S compensation topology. This significantly increases the number of passive components required for the system design, elevating the overall cost and power losses. In view of this, Wang et al. [24] presented a reconstructed S-*LCC* topology that can achieve dual-type constant outputs functionality with fewer compensation components. Despite the simplicity of the reconstructed S-*LCC* topology, which aligns with the design requirements for small size and low cost, it is incapable of achieving dual CV outputs, making it inappropriate for industrial power supply applications. Furthermore, this topology does not support independent adjustment of the charging levels at both output ports, and the CC output is constrained by loosely coupled transformer (LCT) parameters, significantly diminishing its flexibility.

This manuscript proposes a novel compensation topology that delivers independently regulatable dual CV outputs without complex closed-loop control strategies. The proposed structure significantly reduces the number of passive components on the premise of flexibly adjusting the dual CV outputs through the compensation component parameters without complex control, which further ensures the low cost and high flexibility of the system. Both simulation and experimental validation support the viability of the proposed system.

The rest of this article is organized as follows: Section II presents a theoretical analysis of the proposed novel compensation topology, highlighting its independently adjustable dual CV output characteristics and the associated zero-phase-angle (ZPA) operation. Then, Section III describes the detailed parameter design method of the proposed IPT system, and verifies the dual CV output characteristics and ZPA operation through simulation. Furthermore, to reduce the switching losses of MOSFETs in the high-frequency inverter (HFI), the conditions for achieving zero-voltage switching (ZVS) and the sensitivity of dual-output voltage to compensation component parameter variations are rigorously analyzed and discussed. In Section IV, an experimental prototype is implemented, delivering a 40-V CV output on Port 1 and a 60-V CV output on Port 2, thus thoroughly demonstrating the practicality of the proposed IPT system in terms of dual CV output performance, ZPA operation, and ZVS operation. In addition, several other typical multiple outputs IPT systems are introduced for comparison, offering a clearer perspective on the functional and structural advantages of the proposed IPT system. Finally, Section V concludes this article.

II. Theoretical Analysis

The circuit configuration of the proposed IPT system is depicted in Fig. 1. In this configuration, U_{D} represents the dc input voltage source, which primarily powers an HFI comprising four MOSFETs (Q_1–Q_4). The inductance of the transmitting coil is symbolized by L_{P}, while L_{S} denotes the inductance of the receiving coil. The transmitter's resonant capacitor is represented by C_{P}. On the receiving side, compensation inductances are indicated by L_1 and L_2, while resonant capacitors are denoted

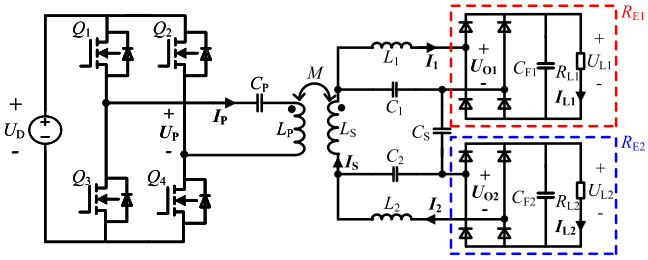

Fig. 1. Circuit scheme of the proposed IPT system with dual CV outputs.

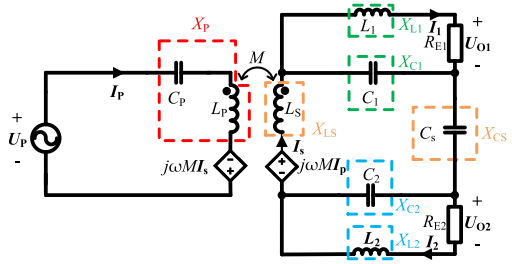

Fig. 2. Simplified equivalent circuit of the proposed IPT system.

by C_1, C_2, and C_{S}. C_{F1} and C_{F2} serve as filter capacitors for the receiving end. R_{L1} and R_{L2} represent the equivalent resistances of the two loads, and the mutual inductance between the transmitting and receiving coils is represented by M. The output voltage phasor of the HFI is denoted as $\boldsymbol{U}_{\mathrm{P}}$, while U_{O1} and U_{O2} denote the input voltage phasors of the rectifiers. The phasors for the currents flowing through various loops in the circuit are expressed as $\boldsymbol{I}_{\mathrm{P}}$, $\boldsymbol{I}_{\mathrm{S}}$, $\boldsymbol{I}_1$, and $\boldsymbol{I}_2$, respectively. The two full-bridge rectifiers consist of two sets of diodes, which convert the ac currents $\boldsymbol{I}_1$ and $\boldsymbol{I}_2$ into dc charging currents I_{L1} and I_{L2} to provide power to the load. In addition, R_{E1} and R_{E2} represent the equivalent ac loads defined by the regions within the red and blue dashed lines, respectively.

The simplified circuit model, as shown in Fig. 2, can be obtained based on the fundamental harmonic approximation method. According to the method outlined in [25], the root mean square (RMS) value of $\boldsymbol{U}_{\mathrm{P}}$ can be expressed as follows:

$$U_{\mathrm{P}} = \frac{2\sqrt{2}}{\pi} U_{\mathrm{D}}. \tag{1}$$

The ac equivalent resistances R_{E1} and R_{E2} may be deduced as follows:

$$\begin{cases} R_{\mathrm{E1}} = \frac{8R_{\mathrm{L1}}}{\pi^2} \\ R_{\mathrm{E2}} = \frac{8R_{\mathrm{L2}}}{\pi^2} \end{cases}. \tag{2}$$

Moreover, the mathematical function relating the system output voltages U_{L1} and U_{L2} to the RMS values of the rectifier input voltages U_{O1} and U_{O2} can be given as follows:

$$\begin{cases} \boldsymbol{U}_{\mathrm{O1}} = \frac{2\sqrt{2}}{\pi} U_{\mathrm{L1}} \\ \boldsymbol{U}_{\mathrm{O2}} = \frac{2\sqrt{2}}{\pi} U_{\mathrm{L2}} \end{cases}. \tag{3}$$

The system operates at a frequency of f, which is mathematically related to the angular frequency by the expression $\omega = 2\pi f$. Utilizing Kirchhoff's voltage law allows for the derivation

of the equations as follows:

$$\begin{cases} j\left(\omega L_{\mathrm{P}}-\frac{1}{\omega C_{\mathrm{P}}}\right)\boldsymbol{I}_{\mathrm{P}}-j\omega M\boldsymbol{I}_{\mathrm{S}}=\boldsymbol{U}_{\mathrm{P}} \\ \left[j\left(\omega L_1-\frac{1}{\omega C_1}\right)+R_{\mathrm{E1}}\right]\boldsymbol{I}_1-j\left(-\frac{1}{\omega C_1}\right)\boldsymbol{I}_{\mathrm{S}}=0 \\ -j\omega M\boldsymbol{I}_{\mathrm{P}}-j\left(-\frac{1}{\omega C_1}\right)\boldsymbol{I}_1-j\left(-\frac{1}{\omega C_2}\right)\boldsymbol{I}_2 \\ \quad +j\left(\omega L_{\mathrm{S}}-\frac{1}{\omega C_{\mathrm{S}}}-\frac{1}{\omega C_1}-\frac{1}{\omega C_2}\right)\boldsymbol{I}_{\mathrm{S}}=0 \\ -j\left(-\frac{1}{\omega C_2}\right)\boldsymbol{I}_{\mathrm{S}}+\left[j\left(\omega L_1-\frac{1}{\omega C_2}\right)+R_{\mathrm{E2}}\right]\boldsymbol{I}_2=0 \end{cases}. \tag{4}$$

For facilitating ZPA operation, the following equations should be satisfied. ZPA operation ensures that the input impedance of the system is purely resistive, thereby improving power transfer efficiency and reducing reactive power

$$\begin{cases} \omega L_{\mathrm{P}}-\frac{1}{\omega C_{\mathrm{P}}}=0 \\ \omega L_1-\frac{1}{\omega C_1}=0 \\ \omega L_2-\frac{1}{\omega C_2}=0 \\ \omega L_{\mathrm{S}}-\frac{1}{\omega C_S}-\frac{1}{\omega C_1}-\frac{1}{\omega C_2}=0 \end{cases}. \tag{5}$$

Substituting (5) into (4), the current phasors $\boldsymbol{I}_{\mathrm{P}}$, $\boldsymbol{I}_1$, and $\boldsymbol{I}_2$ can be solved

$$\begin{cases} \boldsymbol{I}_{\mathrm{P}}=\frac{\boldsymbol{U}_{\mathrm{P}}(R_{\mathrm{E1}}C_1+R_{\mathrm{E2}}C_2)}{R_{\mathrm{E1}}R_{\mathrm{E2}}C_2C_1^2M^2\omega^4} \\ \boldsymbol{I}_1=\frac{\boldsymbol{U}_{\mathrm{P}}L_1}{R_{\mathrm{E1}}M} \\ \boldsymbol{I}_2=\frac{\boldsymbol{U}_{\mathrm{P}}L_2}{R_{\mathrm{E2}}M} \end{cases}. \tag{6}$$

The dual output voltages ($\boldsymbol{U}_{\mathrm{O1}}$ and $\boldsymbol{U}_{\mathrm{O2}}$) of the system can be derived as follows:

$$\begin{cases} \boldsymbol{U}_{\mathrm{O1}}=\frac{\boldsymbol{U}_{\mathrm{P}}L_1}{M} \\ \boldsymbol{U}_{\mathrm{O2}}=\frac{\boldsymbol{U}_{\mathrm{P}}L_2}{M} \end{cases}. \tag{7}$$

From (7), it can be observed that the dual output voltages, $\boldsymbol{U}_{\mathrm{O1}}$ and $\boldsymbol{U}_{\mathrm{O2}}$, remain unaffected by resistive load variations. The desired voltage levels can be attained by independently regulating the compensation inductors L_1 and L_2, free from the constraints imposed by LCT parameters.

In addition, from (6), the expression for the input impedance of the system can be derived

$$Z_{\mathrm{in}}=\frac{R_{\mathrm{E1}}R_{\mathrm{E2}}C_2C_1^2M^2\omega^4}{R_{\mathrm{E1}}C_1+R_{\mathrm{E2}}C_2}. \tag{8}$$

As demonstrated by (8), Z_{in} exhibits a purely resistive characteristic, signifying the completion of ZPA operation. This feature efficiently avoids extra losses caused by high-frequency reactive currents, thus ensuring the system's power transfer efficiency.

In summary, the proposed IPT system facilitates load-independent dual CV output under ZPA operating conditions. According to the method proposed in [26], dual CC outputs or both CC output and CV output can be obtained by simply cascading the T-type resonant circuit at the end of the proposed compensation topology.

III. Simulation Verification and ZVS Implementation

A. Simulation Verification

The parameter design process for this system is shown in Fig. 3. In practical applications, certain multiple-output IPT systems are characterized by specific fixed parameters, including the dc input voltage, operating frequency, and output voltages. In this study, the dc input voltage U_{D} is set at 60 V, while the operating frequency f is specified at 85 kHz. Moreover, the expected output voltages for the two output channels are $U_{\mathrm{L1}}=60$ V and $U_{\mathrm{L2}}=40$ V, respectively. Based on prior theoretical analysis and this design flow, simulation parameters are designed as listed in Table I.

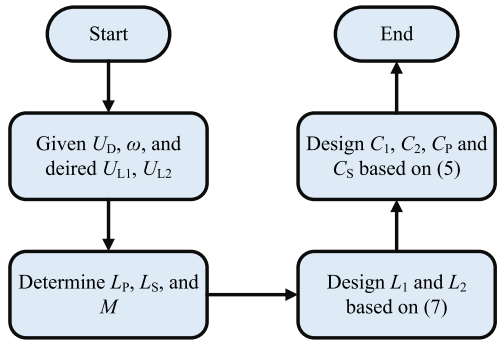

Fig. 3. Simplified equivalent circuit of the proposed IPT system.

TABLE I
Simulation Parameters of the System

Parameters	Value	Parameters	Value	Parameters	Value	Parameters	Value
U_{D}(V)	60	$L_1(\mu$H)	30	f(kHz)	85	C_1(nF)	116.86
$L_{\mathrm{P}}(\mu$H)	100	$L_2(\mu$H)	20	C_{P}(nF)	35.06	C_2(nF)	175.3
$L_{\mathrm{S}}(\mu$H)	100	$M(\mu$H)	30	C_{S}(nF)	72.22	-	-

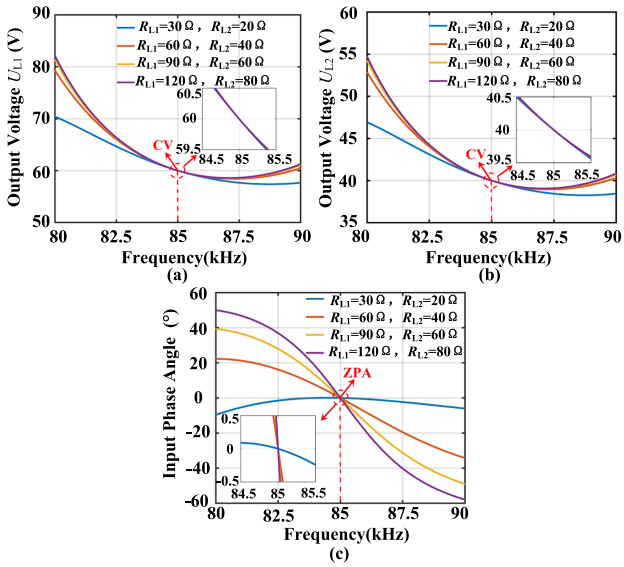

Fig. 4. Variations in dual output voltages (a) U_{L1}, (b) U_{L2}, and (c) input phase angles with frequency under diverse resistive load conditions.

Fig. 4 depicts the variations in dual output voltages and input phase angles with frequency under diverse resistive load conditions. The blue curve corresponds to load resistances of $R_{\mathrm{L1}}=30\ \Omega$ and $R_{\mathrm{L2}}=20\ \Omega$, while the orange curve represents $R_{\mathrm{L1}}=60\ \Omega$ and $R_{\mathrm{L2}}=40\ \Omega$. The yellow curve is associated with load resistances of $R_{\mathrm{L1}}=90\ \Omega$ and $R_{\mathrm{L2}}=60\ \Omega$, and finally, the purple curve is linked to $R_{\mathrm{L1}}=120\ \Omega$ and $R_{\mathrm{L2}}=80\ \Omega$. As observed from Fig. 4(a), the four curves representing

different load resistance conditions intersect at the 85 kHz frequency point, indicating that output port 1 achieves a CV output independent of the load. Similarly, Fig. 4(b) shows that output port 2 also realizes a load-independent CV output. Furthermore, Fig. 4(c) illustrates that the four curves corresponding to different load resistance conditions intersect at the 85 kHz frequency point, with the system's input phase angle at that point being zero. This signifies that the system can perform ZPA operation, effectively avoiding additional losses caused by high-frequency reactive circulating currents, thus improving the overall energy transmission efficiency of the system.

In summary, all curves converge to a point at 85 kHz, respectively, in Fig. 4(a)–(c) where the system's input phase angle is zero. This convergence validates the IPT system's capability to deliver dual CV outputs under ZPA conditions, confirming the accuracy of previous theoretical analysis.

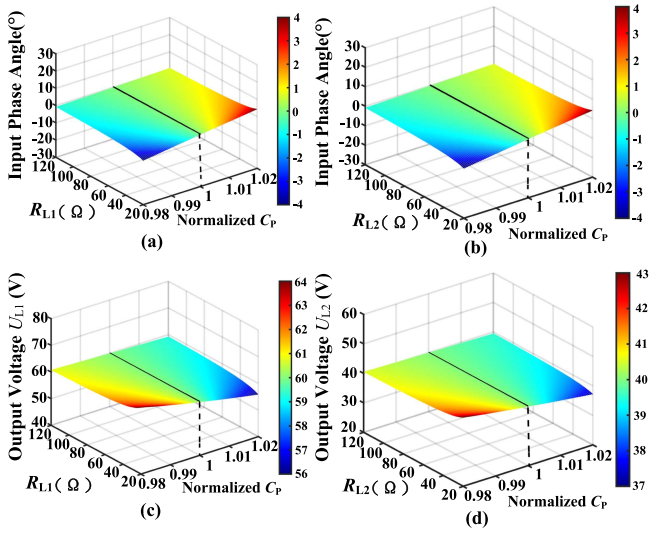

Fig. 5. Variation of output voltages or input phase angle versus the varying normalized compensation capacitor C_P at different load resistances. (a) Variation of U_{L1} versus the normalized C_P at varying R_{L1}. (b) Variation of U_{L2} versus the normalized C_P at varying R_{L2}. (c) Variation of the input phase angle versus the normalized C_P at varying R_{L1}. (d) Variation of the input phase angle versus the normalized C_P at varying R_{L2}.

B. ZVS Implementation

In practical applications, achieving ZVS operation is critical for reducing switching losses and enhancing the overall efficiency of the IPT system. This can be accomplished by configuring the input impedance of the system to exhibit a slight inductive characteristic, which effectively compensates for the parasitic capacitance of the MOSFETs.

Based on the ZPA operation depicted in Fig. 4, the fine adjustment of either the operating frequency [27], [28] or the parameter value of a compensation component [29], [30] allows for the implementation of ZVS operation. As shown in Fig. 4(a) and (b), reducing the operating frequency does not compromise the load-independent dual CV output characteristic. However, Fig. 4(c) reveals that the system's input impedance exhibits slightly inductive behavior only under light-load conditions, while it becomes capacitive under heavy-load conditions, failing to achieve ZVS. Therefore, the methodology employed in this research is the latter. Notably, the specific choice of which compensation component parameter to fine-tune for achieving ZVS operation requires a comprehensive consideration based on the sensitivity of the system's input phase angle and dual CV output characteristics to changes in compensation component parameters. The effects of normalized compensation component adjustments and different load resistances on the output voltages and input phase angle are analyzed as follows.

Figs. 5–10 illustrate the impact of variations in compensation component parameters on dual output voltages and input phase angles under varying load resistances R_{L1} and R_{L2}. From Figs. 5(a) and (b) to 7(a) and (b), it is evident that C_P, L_1, and L_2 are positively correlated with the input phase angle. Similarly, Fig. 8(a) and (b) to 10(a) and (b) reveal that C_1, C_2, and C_S are negatively correlated with the input phase angle. Therefore, achieving ZVS operation may be feasible by increasing C_P, L_1, or L_2, or by reducing C_1, C_2, or C_S. Nevertheless, altering these parameters might lead to output voltage instability, making it necessary to identify the component whose adjustment minimally affects output voltage. From Fig. 5(c) and (d), C_P exhibits a significant impact on both U_{L1} and U_{L2}. Figs. 6(c) and (d) to 9(c) and (d) reveal that changes in L_1, L_2, C_1, and C_2 also produce considerable disturbances in one of the dual output voltages. Conversely, Fig. 10(c) and (d) show that changes in C_S produce almost no effect on either U_{L1} or U_{L2}. In conclusion, minorly reducing the value of C_S can make the input impedance of the system slightly inductive to achieve ZVS operation without affecting the characteristics of the dual CV outputs.

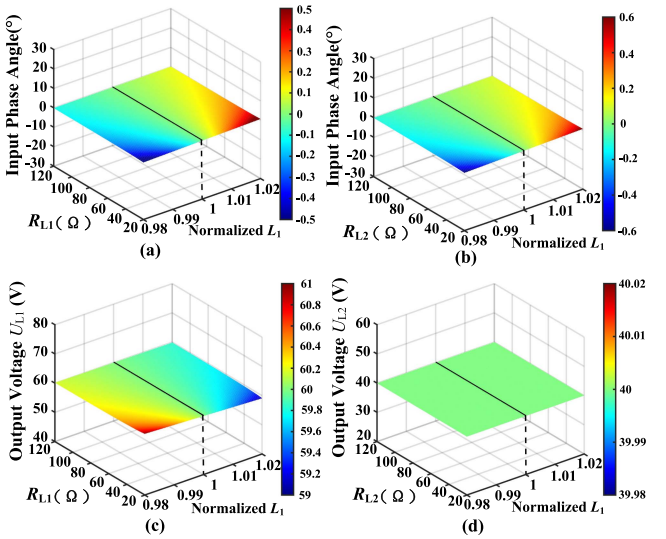

Fig. 6. Variation of output voltages or input phase angle versus varying the normalized compensation inductor L_1 at different load resistances. (a) Variation of U_{L1} versus the normalized L_1 at varying R_{L1}. (b) Variation of U_{L2} versus the normalized L_1 at varying R_{L2}. (c) Variation of the input phase angle versus the normalized L_1 at varying R_{L1}. (d) Variation of the input phase angle versus the normalized L_1 at varying R_{L2}.

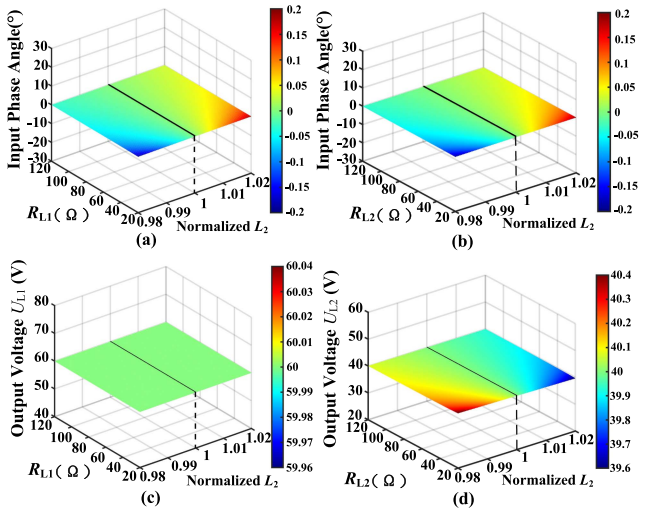

Fig. 7. Variation of output voltages or input phase angle versus varying the normalized compensation inductor L_2 at different load resistances. (a) Variation of U_{L1} versus the normalized L_2 at varying R_{L1}. (b) Variation of U_{L2} versus the normalized L_2 at varying R_{L2}. (c) Variation of the input phase angle versus the normalized L_2 at varying R_{L1}. (d) Variation of the input phase angle versus the normalized L_2 at varying R_{L2}.

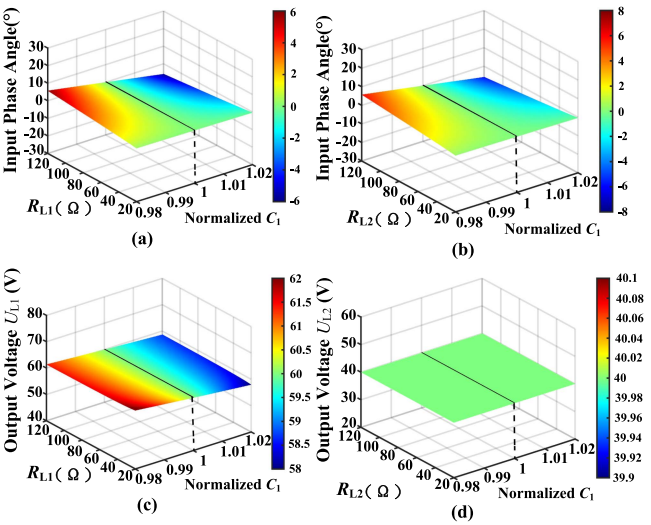

Fig. 8. Variation of output voltages or input phase angle versus varying the normalized compensation capacitor C_1 at different load resistances. (a) Variation of U_{L1} versus the normalized C_1 at varying R_{L1}. (b) Variation of U_{L2} versus the normalized C_1 at varying R_{L2}. (c) Variation of the input phase angle versus the normalized C_1 at varying R_{L1}. (d) Variation of the input phase angle versus the normalized C_1 at varying R_{L2}.

IV. Experimental Verification

A. Experimental Prototype

To verify the performance of the proposed IPT system, an experimental prototype with dual CV outputs (U_{L1} = 60 V and U_{L2} = 40 V) is constructed according to the previous theoretical analysis, and its parameters are listed in Table II. As shown in Fig. 11, the prototype consists of the voltage source, inverter, transmitting compensation circuit (L_P and C_P), LCT (composed of ferrite (PC 40) and two rounded square coils),

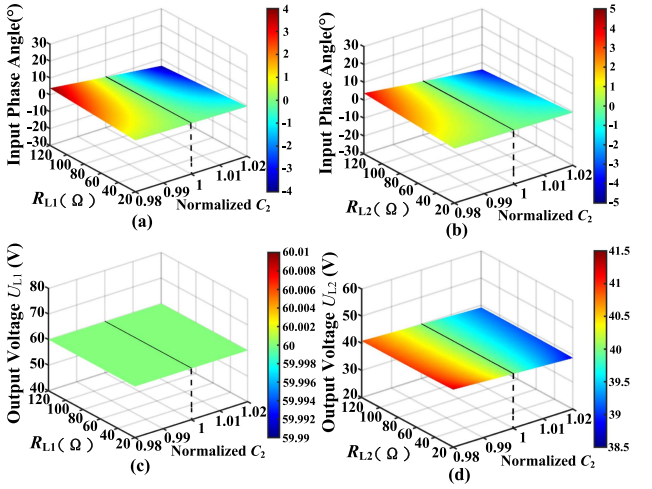

Fig. 9. Variation of output voltages or input phase angle versus varying the normalized compensation capacitor C_2 at different load resistances. (a) Variation of U_{L1} versus the normalized C_2 at varying R_{L1}. (b) Variation of U_{L2} versus the normalized C_2 at varying R_{L2}. (c) Variation of the input phase angle versus the normalized C_2 at varying R_{L1}. (d) Variation of the input phase angle versus the normalized C_2 at varying R_{L2}.

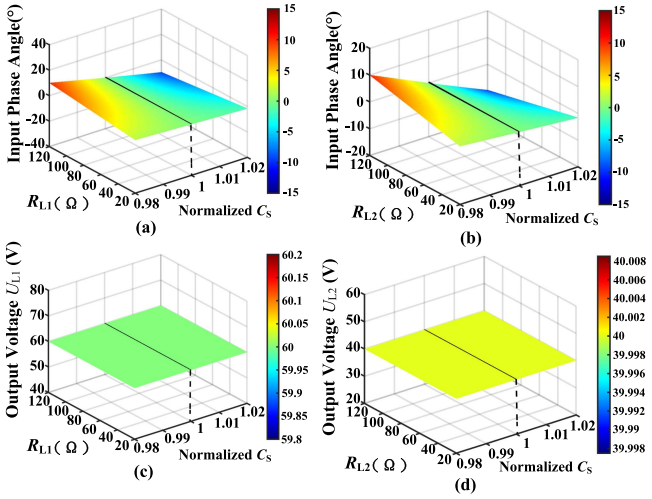

Fig. 10. Variation of output voltages or input phase angle versus varying the normalized compensation capacitor C_S at different load resistances. (a) Variation of U_{L1} versus the normalized C_S at varying R_{L1}. (b) Variation of U_{L2} versus the normalized C_S at varying R_{L2}. (c) Variation of the input phase angle versus the normalized C_S at varying R_{L1}. (d) Variation of the input phase angle versus the normalized C_S at varying R_{L2}.

TABLE II
Measured Parameters of the System

Parameters	Value	Parameters	Value	Parameters	Value	Parameters	Value
U_D(V)	60	L_1(μH)	30.04	f(kHz)	85	C_1(nF)	116.71
L_P(μH)	100.1	L_2(μH)	20.06	C_P(nF)	35.02	C_2(nF)	174.77
L_S(μH)	100.3	M(μH)	30.05	C_S(nF)	71.94	C_{S_ZVS}(nF)	69.84

receiving compensation circuit (L_S, C_S, L_1, C_1, L_2, and C_2), two rectifiers and two load resistors (R_{L1} and R_{L2}). In the designed IPT system, coil windings are made from Litz wire with 400 strands and 2.8 mm diameter to reduce the equivalent series resistance and skin effect. The inner and outer diameters of the

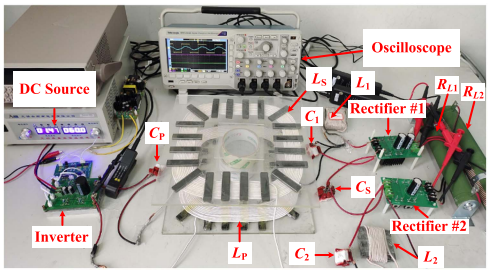

Fig. 11. Experimental prototype of the proposed system.

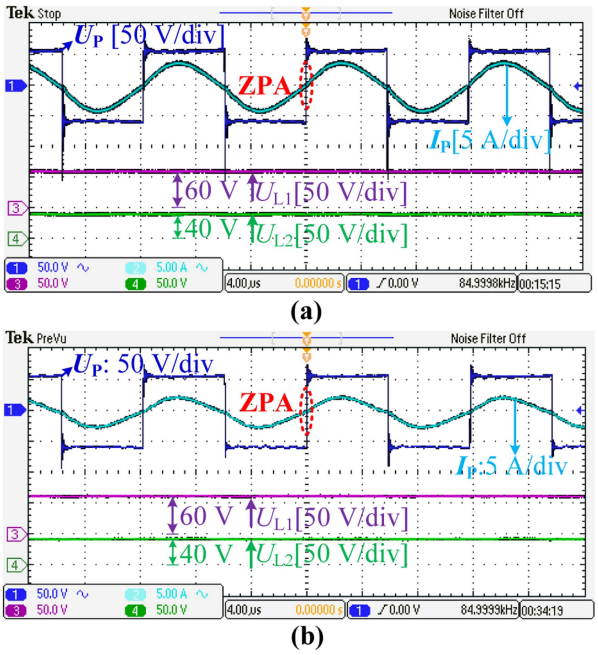

Fig. 12. Measured waveforms of the proposed IPT system under ZPA condition at different load resistances. (a) $R_{L1} = 40\ \Omega$ and $R_{L2} = 30\ \Omega$. (b) $R_{L1} = 80\ \Omega$ and $R_{L2} = 60\ \Omega$.

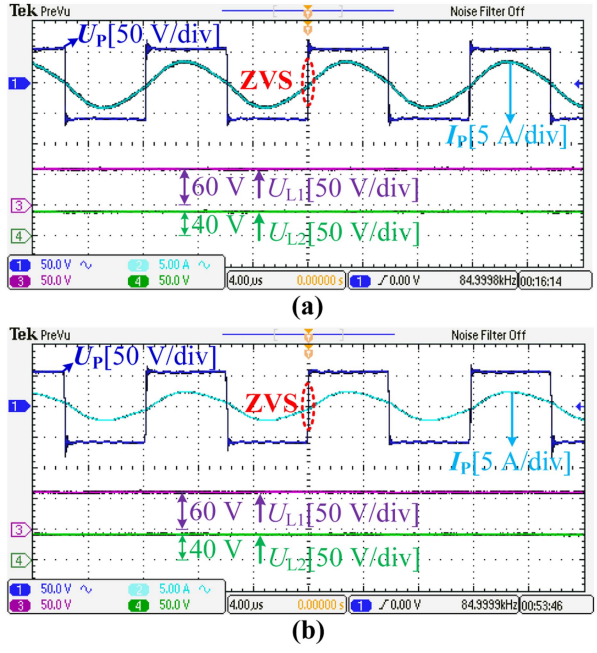

Fig. 13. Measured waveforms of the proposed IPT system under ZVS condition at different load resistances. (a) $R_{L1} = 40\ \Omega$ and $R_{L2} = 30\ \Omega$. (b) $R_{L1} = 80\ \Omega$ and $R_{L2} = 60\ \Omega$.

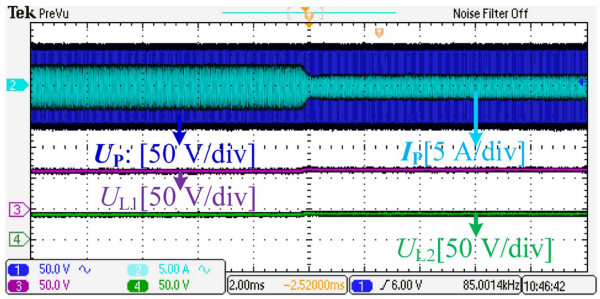

Fig. 14. Dynamic response waveforms of the proposed IPT system when step changes of the load resistances R_{L1} and R_{L2} occur.

transmitting and receiving coils are the same, 262 and 186 mm, respectively, and the air gap between the coils is 75 mm. Owing to its inherent structural attributes, the proposed topology enables independently dual CV outputs without resorting to sophisticated control techniques. Therefore, similar to the approaches in [17], [18], [19], [20], [21], [22], [23], [24], on the premise that the dc input voltage is constant, a simple STM32F103 controller can be employed to generate the switching signals to control the complementary conduction of Q_1/Q_4 and Q_2/Q_3 with a 50% duty cycle, enabling the proposed system maintains stable dual CV output characteristics.

B. Experimental Results

Fig. 12 shows the waveforms of the inverter voltage $\boldsymbol{U}_{\mathrm{P}}$, current $\boldsymbol{I}_{\mathrm{P}}$ and dual output voltages U_{L1} and U_{L2}. It is observed that the input voltage $\boldsymbol{U}_{\mathrm{P}}$ and current $\boldsymbol{I}_{\mathrm{P}}$ of the system are almost in the same phase, verifying the implementation of ZPA operation. When the load resistance changes from $R_{\mathrm{L1}} = 40\ \Omega$ and $R_{\mathrm{L2}} = 30\ \Omega$ as shown in Fig. 12(a) to $R_{\mathrm{L1}} = 80\ \Omega$ and $R_{\mathrm{L2}} = 60\ \Omega$ as shown in Fig. 12(b), the output voltages U_{L1} and U_{L2} remain essentially stable at 60 and 40 V, respectively, verifying the dual CV output characteristics of the proposed IPT system.

Compared to Fig. 12, C_{S} is adjusted to $C_{\mathrm{S\_ZVS}}$ while keeping all other conditions the same in Fig. 13. It can be observed that the input voltage $\boldsymbol{U}_{\mathrm{P}}$ slightly leads the input current $\boldsymbol{I}_{\mathrm{P}}$, confirming the completion of ZVS operation. Notably, the dual output voltages in Figs. 12 and 13 remain substantially constant, indicating that the proposed system is capable of achieving ZVS operation without affecting the dual CV outputs.

Fig. 14 presents the dynamic response waveforms of the proposed IPT system when step changes of the load resistances R_{L1} and R_{L2} occur. As evident from Fig. 14, when the load conditions suddenly change from $R_{\mathrm{L1}} = 40\ \Omega$ and $R_{\mathrm{L2}} = 30\ \Omega$ to $R_{\mathrm{L1}} = 80\ \Omega$ and $R_{\mathrm{L2}} = 60\ \Omega$, the output voltages U_{L1} and U_{L2} show minimal fluctuation, remaining stable at approximately 60 and 40 V, respectively. These dynamic response results further affirm that the proposed system is capable of stably delivering two independent CV outputs.

TABLE III
COMPARISON OF THIS WORK WITH OTHER PREVIOUS MULTI-OUTPUT SYSTEMS

Proposed in	[13]	[14]	[15]	[16]	[17]	[18]	[19]	[20]	[21]	[22]	[23]	[24]	This work
Number of transmitting coils	1	1	2	2	1	1	2	1	1	1	1	1	1
Number of receiving coils	1	1	2	2	2	2	2	2	1	1	1	1	1
Number of receiver compensation components	3	1	2	2	2	2	6	3	8	8	14	3	5
Without DC-DC converters	No	No	Yes	Yes	Yes	Yes	Yes	Yes	Yes	Yes	Yes	Yes	Yes
Without decoupling strategies	Yes	Yes	Yes	Yes	Yes	No	No	No	Yes	Yes	Yes	Yes	Yes
Independently regulatable dual outputs	No	No	No	No	No	No	Yes	No	Yes	Yes	Yes	No	Yes
DC-DC peak efficiency	90.36%	90%	54.72%	90.1%	78%	90.16%	94.07%	93.2%	89.33%	88%	91.12%	94.95%	92.8%

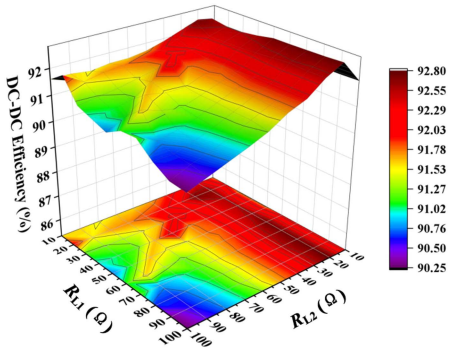

Fig. 15. Overall DC–DC efficiency of the proposed IPT system against varying load resistances R_{L1} and R_{L2}.

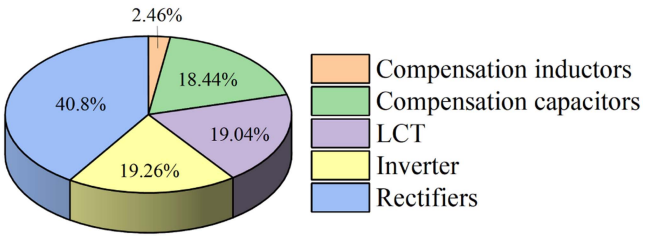

Fig. 16. Power loss distribution of the proposed system at the peak efficiency point.

The overall dc–dc efficiency of the proposed IPT system against varying load resistances is measured, as depicted in Fig. 15. It is evident that as the load resistances change, the efficiency of the system remains at a relatively high level, with a peak value of 92.8%.

Power loss distribution of the proposed system at the peak efficiency point is illustrated in Fig. 16. Rectifiers and inverter losses account for the majority of the total power losses. Therefore, the rational selection of semiconductor devices is crucial for improving efficiency.

To more clearly highlight the superior performance of the proposed IPT system, a comparative analysis with other previous multioutput systems is presented in Table III. From this comparison, the following conclusions can be drawn:

1) Differing from the methodologies presented in [13] and [14], the approach proposed in this manuscript does not require cascading additional dc–dc converters, thus maintaining system cost-effectiveness while reducing unnecessary power losses.

2) The proposal in this manuscript adopts a single transmitter and single receiver structure. It does not require consideration of cross-coupling interference among coils as researches in [15], [16], [17] and avoids the introduction of decoupling strategies like studies in [18], [19], [20], thereby facilitating more flexible magnetic coupler design.

3) Compared with the studies in [21], [22], [23], the proposed compensation topology significantly reduces the number of passive components, which implies higher cost-effectiveness and lower power losses of the system.

4) Despite the simplicity of the reconstructed S-LCC topology described in [24], the system output is limited by the LCT parameters, thus preventing independent adjustment of dual outputs. In contrast, the system introduced in this manuscript can independently regulate the dual outputs by adjusting the corresponding compensation component parameters, ensuring the flexibility of the system.

V. CONCLUSION

This manuscript proposes a novel compensation topology capable of achieving independent regulatable dual CV outputs by exploiting its inherent structural attributes. The proposed system features a streamlined design that does not require complex closed-loop control strategies. It simply requires adjustments to the compensation component parameters to achieve the desired independent dual CV outputs, thereby ensuring system flexibility. Compared with previous works on similar systems, this methodology employs fewer compensation components without compromising flexibility. Consequently, the proposed system significantly reduces development costs and power losses. The experimental results prove the dual CV output characteristics of the proposed system under ZPA and ZVS operating conditions.

REFERENCES

[1] J. Wanget al., "Tri-coupled dual-LCC compensation network for wireless charging of AUVs with high misalignment tolerance," *IEEE Trans. Power Electron.*, vol. 40, no. 9, pp. 14124–14133, Sep. 2025, doi: 10.1109/TPEL.2025.3568836.

[2] L. Yang, Y. Wang, P. Guo, K. Dong, and C. Cai, "A reconfigurable rectifier based communication-free wireless LED driver with dual-customization CC outputs," *IEEE Trans. Power Electron.*, vol. 40, no. 2, pp. 2680–2684, Feb. 2025.

[3] J. Li, J. Zhu, J. Xie, F. Lu, and X. Zhang, "Design and implementation of high-misalignment tolerance WPT system for underwater vehicles based on a variable inductor," *IEEE Trans. Power Electron.*, vol. 38, no. 10, pp. 11726–11737, Oct. 2023.

[4] S. Roy, A. Azad, S. Baidya, M. Alam, and F. Khan, "Powering solutions for biomedical sensors and implants inside the human body: A comprehensive review on energy harvesting units, energy storage, and wireless power transfer techniques," *IEEE Trans. Power Electron.*, vol. 37, no. 10, pp. 12237–12263, Oct. 2022.

[5] H. Shenget al., "A soft implantable energy supply system that integrates wireless charging and biodegradable Zn-ion hybrid supercapacitors," *Sci. Adv.*, vol. 9, no. 46, Nov. 2023, Art. no. eadh8083.
[6] C. Liu, C. Jiang, Z. Jin, and K. Chau, "An effective sandwiched wireless power transfer system for charging implantable cardiac pacemaker," *IEEE Trans. Ind. Electron.*, vol. 66, no. 5, pp. 4108–4117, May 2019.
[7] C. Gaoet al., "A seamlessly integrated device of micro-supercapacitor and wireless charging with ultrahigh energy density and capacitance," *Nature Commun.*, vol. 12, no. 1, May 2021, Art. no. 2647.
[8] Y. Zhang, S. Chen, X. Li, and Y. Tang, "Design methodology of free-positioning nonoverlapping wireless charging for consumer electronics based on antiparallel windings," *IEEE Trans. Ind. Electron.*, vol. 69, no. 1, pp. 825–834, Jan. 2022.
[9] Y. Liu, C. Liu, Z. Dong, S. Li, and W. Wang, "A novel wireless energy router for home energy management with omnidirectional power transmission," *IEEE Trans. Ind. Electron.*, vol. 70, no. 9, pp. 8979–8990, Sep. 2023.
[10] H. Xu, J. Wang, and Z. Huang, "Large-spacing segmented transmitter track for dynamic wireless power transfer with low output fluctuation," *IEEE Trans. Power Electron.*, vol. 40, no. 9, pp. 14134–14145, Sep. 2025, doi: 10.1109/TPEL.2025.3569698.
[11] W. Pan et al., "An adaptive and scalable wireless charging system for electric vehicles with enhanced interoperability and misalignment tolerance," *IEEE Trans. Power Electron.*, vol. 40, no. 9, pp. 14159–14168, Sep. 2025, doi: 10.1109/TPEL.2025.3571803.
[12] J. Li, F. Chen, R. Zhu, Y. Chen, and R. Mai, "3-D embedded receiving coil positioning based on decoupled transformer for wireless sensor power supply system," *IEEE Trans. Power Electron.*, early access, doi: 10.1109/TPEL.2025.3566391.
[13] J. Huet al., "Hybrid energy storage system of an electric scooter based on wireless power transfer," *IEEE Trans. Ind. Inform.*, vol. 14, no. 9, pp. 4169–4178, Sep. 2018.
[14] M. Matthew, "Integration of inductively coupled power transfer and hybrid energy storage system: A multiport power electronics interface for battery-powered electric vehicles," *IEEE Trans. Power Electron.*, vol. 30, no. 11, pp. 6423–6433, Nov. 2015.
[15] M. Nguyen, Y. Chou, D. Plesa, S. Rao, J. Chiao, and J. Chiao, "Multiple-inputs and multiple-outputs wireless power combining and delivering systems," *IEEE Trans. Power Electron.*, vol. 30, no. 11, pp. 6254–6263, Nov. 2015.
[16] Q. Duong and O. Minoru, "Maximum efficiency formulation for multiple-input multiple-output inductive power transfer systems," *IEEE Trans. Microw. Theory Techn.*, vol. 66, no. 7, pp. 3463–3477, Jul. 2018.
[17] M. Ahn and P. P. Mercier, "Wireless power transfer with concurrent 200 kHz and 6.78 MHz operation in a single-transmitter device," *IEEE Trans. Power Electron.*, vol. 31, no. 7, pp. 5018–5029, Jul. 2016.
[18] H. Wang and K. W. E. Cheng, "Analysis, design, and validation of a decoupled double-receiver wireless power transfer system with constant voltage outputs for industrial power supplies," *IEEE Trans. Ind. Informat.*, vol. 19, no. 1, pp. 362–370, Jan. 2023.
[19] Y. Li, T. Lin, R. Mai, L. Huang, and Z. He, "Compact double-sided decoupled coils-based WPT systems for high-power applications: Analysis, design, and experimental verification," *IEEE Trans. Transport. Electrific.*, vol. 4, no. 1, pp. 64–75, Mar. 2018.
[20] R. Mai, Y. Luo, B. Yang, Y. Song, S. Liu, and Z. He, "Decoupling circuit for automated guided vehicles IPT charging systems with dual receivers," *IEEE Trans. Power Electron.*, vol. 35, no. 7, pp. 6652–6657, Jul. 2020.
[21] Y. Li, J. Hu, X. Liu, Q. Xu, and R. Mai, "Analysis, design, and experimental verification of a mixed high-order compensations-based WPT system with constant current outputs for driving multistring LEDs," *IEEE Trans. Ind. Electron.*, vol. 67, no. 1, pp. 203–213, Jan. 2020.
[22] Y. Li, J. Hu, X. Liu, and W. Cheng, "Cost-effective and compact multistring LED driver based on a three-coil wireless power transfer system," *IEEE Trans. Power Electron.*, vol. 34, no. 8, pp. 7156–7160, Aug. 2019.
[23] Y. Li, J. Hu, X. Li, and W. Cheng, "A flexible load-independent multi-output wireless power transfer system based on cascaded double T-resonant circuits: Analysis, design and experimental verification," *IEEE Trans. Circuits Syst. I: Reg. Papers*, vol. 66, no. 7, pp. 2803–2812, Jul. 2019.
[24] X. Wang, J. Xu, H. Ma, and Z. Yan, "A reconstructed S-LCC topology with dual-type outputs for inductive power transfer systems," *IEEE Trans. Power Electron.*, vol. 35, no. 12, pp. 12606–12611, Dec. 2020.
[25] R. Erickson and D. Maksimovic, *Fundamentals of Power Electronics*. Berlin, Germany: Springer Science, 2007.
[26] J. Lu, G. Zhu, D. Lin, Y. Zhang, J. Jiang, and C. Mi, "Unified load-independent ZPA analysis and design in CC and CV modes of higher order resonant circuits for WPT systems," *IEEE Trans. Transport. Electrific.*, vol. 5, no. 4, pp. 977–987, Dec. 2019.
[27] V. Vu, D. Tran, and W. Choi, "Implementation of the constant current and constant voltage charge of inductive power transfer systems with the double-sided LCC compensation topology for electric vehicle battery charge applications," *IEEE Trans. Power Electron.*, vol. 33, no. 9, pp. 7398–7410, Sep. 2018.
[28] D. Tran, B. Vu, and W. Choi, "Design of a high-efficiency wireless power transfer system with intermediate coils for the on-board chargers of electric vehicles," *IEEE Trans. Power Electron.*, vol. 33, no. 1, pp. 175–187, Jan. 2018.
[29] L. Yang, K. Dong, Y. Wang, and C. Cai, "Analysis and design of a dual-receiver WPT system with constant current and constant voltage dual-type outputs," *IEEE Trans. Transport. Electrific.*, vol. 11, no. 1, pp. 4060–4069, Feb. 2025.
[30] S. Ren, X. Wang, J. Xu, and P. Yang, "Primary-side resonant current-/voltage-clamped IPT systems without clamping coil or isolation transformer for inherent CC-to-CV charging," *IEEE Trans. Emerg. Sel. Topics Power Electron.*, vol. 13, no. 1, pp. 1281–1294, Feb. 2025.